Computers and Geotechnics 191 (2026) 107772

Contents lists available at ScienceDirect

Computers and Geotechnics

journal homepage: www.elsevier.com/locate/compgeo

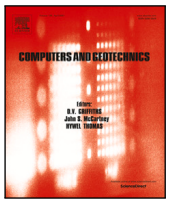

Research paper

An anisotropic semi-micromechanical cyclic constitutive model for sands

Hilmi Bayraktaroglu, Mandy Korff, Michael A. Hicks *

Section of Geo-Engineering, Faculty of Civil Engineering and Geosciences, Delft University of Technology, Delft, The Netherlands

ARTICLE INFO

Keywords:
Fabric anisotropy
Constitutive modelling
Sands
Cyclic loading
Multilaminate framework

ABSTRACT

The anisotropic behaviour of sands, which is associated with their grain-scale microstructural characteristics such as the distribution of voids and the spatial orientation of particles, can lead to significant variations in macro-scale predictions. In this paper, a bounding surface plasticity based anisotropic semi-micromechanical constitutive model is developed, within the multilaminate framework, to describe the effects of fabric on the cyclic behaviour of sands. A novel plastic strain driven semi-micromechanical fabric evolution framework fulfilling the premises of anisotropic critical state theory is proposed. Rather than using a single scalar-valued fabric anisotropic variable, which is the general practise in anisotropic critical state theory based models, independently evolving fabric anisotropic variables are employed at so-called sampling planes. In addition, the semifluidised state concept is utilised at low mean effective stresses to realistically capture post-liquefaction responses, including large shear deformations and accumulative plastic strains during flow liquefaction and cyclic mobility types of behaviour. The procedure for calibrating model parameters is briefly described and the prediction capabilities of the proposed model under drained and undrained monotonic and cyclic loading conditions at different stress states, relative densities and loading orientations are demonstrated by simulating experimental data for Toyoura sand using a single set of parameters.

1. Introduction

The microstructure (i.e. fabric) of sands, which refers to the arrangement of particles, particle groups and void distributions, is induced by different preparation methods/deposition environments and pre-shearing histories, and significantly influences their macroscopic response (Mitchell and Soga, 2005). The arrangement of particles and their interlocking lead to a complex force chain network, which in turn results in direction-dependent (i.e. anisotropic) behaviour. Experimental studies carried out using monotonic hollow cylinder torsional shear tests have shown that the relative orientation between the major principal fabric and loading directions can drastically change the sand's response, turning a dilative behaviour into a contractive one, even under the same stress path (Nakata et al., 1998; Yoshimine et al., 1998; Sivathayalan and Vaid, 2002). Further investigation into the influence of inherent anisotropy on the dynamic behaviour of sands has revealed its significant impact on both the pre- and post-liquefaction phases, altering liquefaction resistance and large shear-strain accumulations, respectively (Nemat and Tobita, 1982; Miura and Toki, 1984; Oda et al., 2001; Chaudhary et al., 2002; Sivathayalan et al., 2015). Even though element test scale laboratory investigations prove the existence of a strong link between inherent fabric anisotropy and the resulting macroscopic response, the acquisition and interpretation of micro-scale information, which is imperative for quantifying both the initial and evolving soil microstructure, is challenging with existing laboratory techniques. In order to overcome this difficulty and enhance the insight gained from macro scale laboratory experiments, the discrete element method (DEM) proposed by Cundall and Strack (1979) has become a widely adopted numerical approach. The latest computational advances in DEM algorithms not only allow for an accurate replication of the various macroscopic responses exhibited by granular materials, but also provide detailed micro-scale information tracing the individual particles and contact forces between them. In this regard, recent DEM studies focusing on the evolving fabric structure have provided a deeper understanding of the fundamental mechanisms of soil liquefaction (Wang and Wei, 2016; Wang et al., 2016, 2019; Wei et al., 2020; Wei and Wang, 2016, 2017; Yang et al., 2022b; Yang and Huang, 2022; Yang et al., 2022c).

All the aforementioned laboratory experiments and physics-based virtual DEM simulations highlight the significant influence of fabric on the mechanical behaviour of sands. Addressing these challenges requires the utilisation of advanced constitutive models that can adequately capture the anisotropic nature of sands. However, the granular nature of sands poses a significant challenge for continuum constitutive models. The multi-scale complexities ranging from the individual

* Corresponding author.
E-mail address: M.A.Hicks@tudelft.nl (M.A. Hicks).

https://doi.org/10.1016/j.compgeo.2025.107772
Received 28 August 2024; Received in revised form 9 November 2025; Accepted 13 November 2025
Available online 4 December 2025

particle characteristics to the organisation of the granular packing and the reconfiguration of the complex internal structure during shearing, commonly referred to as fabric evolution, introduce additional complexity to the already intricate modelling process. One of the widely adopted approaches in the literature for handling this complex behaviour arising from the anisotropic nature of sands is to define a second-order fabric tensor approximating the microstructure. Although it is more reliable and physically consistent to characterise the initial composition of the microstructure based on granular-level observations, such as using the statistical distribution of the inter-particle contact normal directions proposed by Satake (1978), acquiring such data poses significant challenges. As an alternative, a tensorial quantity based on continuum-level phenomenological observations from laboratory tests can be derived (Petalas et al., 2020). Following the description of the initial fabric tensor, an evolution rule describing the changing microstructure needs to be defined. Finally, the idealised quantitative measure of the evolving sand microstructure can be incorporated into existing constitutive formulations to improve the accuracy in predicting the anisotropic response of sands.

Various attempts have been made to incorporate fabric effects into constitutive formulations through the utilisation of fabric tensors. Wan and Guo (2001) proposed an anisotropic stress-dilatancy formulation along with a stress-ratio driven fabric evolution rule. Li and Dafalias (2002) derived a scalar-valued anisotropic state variable that modifies key constitutive components, namely the dilatancy and plastic modulus formulations. Although the model proposed by Li and Dafalias (2002) does not consider fabric evolution, which contradicts recent granular level experimental and numerical observations obtained from X-ray computed tomography (CT) and DEM simulations, it adequately captures the anisotropic response of sands under monotonic loading conditions. However, the uniqueness of the critical state line (CSL) formulation is compromised by its dependence on fabric and loading direction. In order to address these issues, Li and Dafalias (2012) introduced anisotropic critical state theory (ACST), in which the requirements of critical state theory (CST) were expanded to involve fabric ingredients. ACST has paved the way for numerous constitutive formulations and also served as a pivotal milestone in the advancement of constitutive models incorporating anisotropy.

Even though extensive research efforts have been devoted to the development of constitutive models for simulating the cyclic behaviour of sand and numerous constitutive frameworks have been developed, such as bounding surface, subloading surface, hypoplasticity and multisurface models, only a few ACST-based models have been specifically designed to capture the influence of fabric on the cyclic behaviour of sands. This is due to the complex evolution of soil fabric under cyclic loading conditions, which differs from its monotonic counterpart where the fabric gradually approaches its critical state value. Some of the noteworthy ACST-based models investigating the cyclic behaviour of sands can be found in Gao and Zhao (2015), Wang et al. (2020a), Liao and Yang (2021), Zou and Liu (2021), Pan et al. (2022) and Gao et al. (2023). In this paper, an alternative semi-micromechanical fabric evolution rule is proposed, using the multilaminate framework to tackle the challenges arising from complex loading conditions.

In the multilaminate framework, independently evolving constitutive ingredients at predefined sampling planes facilitate a history-dependent anisotropic mobilisation process without mathematical complexity. Furthermore, the adoption of this framework facilitates a diverse range of possibilities for the seamless incorporation of anisotropic behaviour. For example, Pietruszczak and Mroz (2000) introduced a microstructure tensor to characterise varying material properties over the sampling planes (i.e. changing spatial orientations), while Galavi (2007) utilised it to describe an anisotropic failure criterion. However, in these and similar models, anisotropy is incorporated by distributing the scalar material properties across the sampling planes, independent of the loading direction. In this paper, the intrinsic capabilities of the multilaminate framework, such as handling the effect of principal stress rotation and induced anisotropy, have been further extended, by incorporating ACST such that the fabric characteristics and loading directions at each plane are collectively involved in anisotropy formulations. In this regard, the new formulation represents a cyclic extension of the monotonic model proposed by Bayraktaroglu et al. (2023).

Although the aforementioned cyclic constitutive models have addressed important aspects of sand behaviour, they exhibit limitations in predicting the cyclic behaviour of sands upon liquefaction. These limitations become evident when the whole system undergoes a brief yet impactful transient phase characterised by a substantially decreased shear modulus and a concurrent reduction in dilatancy resulting in large plastic deformations. In order to simulate the post-liquefaction behaviour of sands, Elgamal et al. (2003) proposed a constant-volume perfect plastic phase while crossing the phase transformation line (PTL) at low mean effective stresses near liquefaction and continued this phase until a user-defined octahedral shear strain was accumulated. Zhang and Wang (2012) and Wang et al. (2014) introduced the concept of reversible and irreversible dilatancy, and employed a threshold volumetric strain to determine solid and fluid like behaviours. Boulanger and Ziotopoulou (2013) modified the fabric dilatancy tensor proposed by Dafalias and Manzari (2004), and incorporated it not only into the dilatancy formulation, but also within the plastic modulus and elasticity formulations. Recently, Barrero et al. (2020) introduced the semifluidised state concept, defining an additional state variable to degrade the plastic modulus and dilatancy within the semifluidised zone which is determined using a threshold mean effective stress value.

In the present work, the influence of fabric on both the pre- and post-liquefaction behaviours of sands has been investigated using a semi-micromechanical fabric anisotropy formulation and utilising the semifluidised state concept, collectively. First, concise theoretical aspects of the multilaminate framework and the anisotropic elastoplastic constitutive formulation are presented, and then the performance of the proposed constitutive model is tested against experimental data on Toyoura sand. Note that, in this paper, the term 'micro' refers to within sampling planes and that, unless stated otherwise, all stresses are effective, so that prime symbols are omitted.

2. Constitutive framework

2.1. Multilaminate framework and constitutive adaptation

In this paper, the cyclic behaviour of sands is investigated using the multilaminate framework comprising 33 × 2 orthogonally symmetric sampling planes. Unlike the classical continuum approach, where constitutive models are used to create a direct link between the stress and strain tensors, in this multilaminate enhanced framework the proposed constitutive model is employed at each sampling plane to establish a micro-level link between the stress and strain vectors. A schematic of the framework involving 3 out of the 66 sampling planes, the corresponding local coordinate systems and the stress vectors is illustrated in Fig. 1.

In order to establish a consistent relationship between the macro and micro level stresses, the local stress vectors at each sampling plane are calculated by projecting the macroscopic stress tensor $\boldsymbol{\sigma}$ onto each sampling plane and then transferring the resultant traction stress vectors to their local coordinate systems as follows:

$$\boldsymbol{\sigma}_i = \begin{pmatrix} p + \left(\boldsymbol{\sigma}^* \boldsymbol{n}_i\right) \boldsymbol{n}_i \\ \left(\boldsymbol{\sigma}^* \boldsymbol{n}_i\right) \boldsymbol{n}_s \\ \left(\boldsymbol{\sigma}^* \boldsymbol{n}_i\right) \boldsymbol{n}_t \end{pmatrix} = \begin{pmatrix} \sigma_n \\ s \\ t \end{pmatrix} \tag{1}$$

where $\boldsymbol{n}_i$ is the unit normal vector of the ith sampling plane, $\boldsymbol{n}_s$ and $\boldsymbol{n}_t$ are corresponding local shear coordinates determined according to Hasegawa and Bažant (1993), $\boldsymbol{\sigma}^*$ is the deviatoric part of $\boldsymbol{\sigma}$ and p is the mean effective stress. The local normal stress $\boldsymbol{\sigma}_n$ is further decomposed into volumetric and deviatoric parts as $\boldsymbol{\sigma}_n = \boldsymbol{\sigma}_{n,\mathrm{vol}} + \boldsymbol{\sigma}_{n,\mathrm{dev}}$ with $\boldsymbol{\sigma}_{n,\mathrm{vol}} = p$. The components s and t in Eq. (1) represent

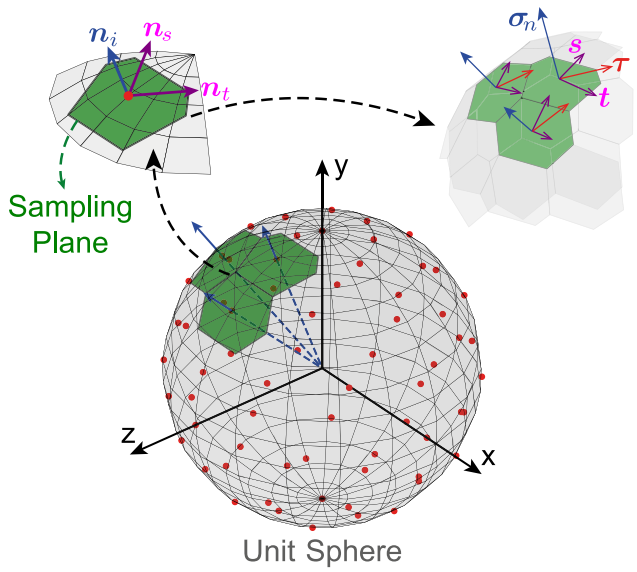

Fig. 1. Schematic of multilaminate framework and local stresses.

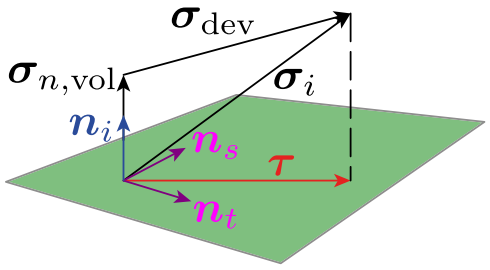

Fig. 2. Volumetric–deviatoric (VD) decomposition of a local stress vector.

the components of the local shear vector in the n_s and n_t directions, respectively. Finally, the local deviatoric stress vector $\boldsymbol{\sigma}_{\mathrm{dev}} = \boldsymbol{\sigma}_i - \boldsymbol{\sigma}_{n,\mathrm{vol}}$ is derived as illustrated in Fig. 2. This process is commonly referred to as the statically constrained volumetric–deviatoric (VD) split method.

Following the derivation of the local stresses, the resistance against shearing/sliding and the resultant volumetric changes, i.e. the local plastic strains, are individually calculated at each sampling plane and then transferred back to their global counterpart through a numerical integration scheme. The collectively derived resultant global plastic strain tensor is used to update the global stress state. Further details and potential advantages of using the multilaminate framework can be found in Bayraktaroglu et al. (2023).

The basics of the new semi-micromechanical model proposed in this paper build on the bounding surface plasticity framework introduced in Dafalias and Manzari (2004), which will be referred to hereafter as SANISAND04. In SANISAND04, constitutive formulations are defined in a tensorial field. However, to utilise this framework within a multilaminate framework, a multilaminate adaptation that downscales the tensorial formulations and constitutive terms to their vectorial counterparts is required. In this regard, the definitions of some of the key constitutive ingredients which are illustrated in Fig. 3 need to be redefined. For the proposed model, this can be accomplished by defining the back-stress ratio vector $\boldsymbol{\alpha}$ and the stress ratio vector $\boldsymbol{r}$, which generalise the slope of the yield surface and the stress ratio, respectively, on a normalised shear plane. Subsequently, the loading direction vector $\boldsymbol{n} = (\boldsymbol{r}-\boldsymbol{\alpha})/|\boldsymbol{r}-\boldsymbol{\alpha}|$ can be utilised to define the direction of the image back-stress ratios. It is important to note that all these quantities are vectors with components defined in the $\boldsymbol{n}_s$ and $\boldsymbol{n}_t$ directions on a normalised shear plane, rather than tensors defined on a deviatoric plane. The decomposition of the local shear vector $\boldsymbol{\tau}$ into $\boldsymbol{s}$ and $\boldsymbol{t}$ is essential to capture loading reversals.

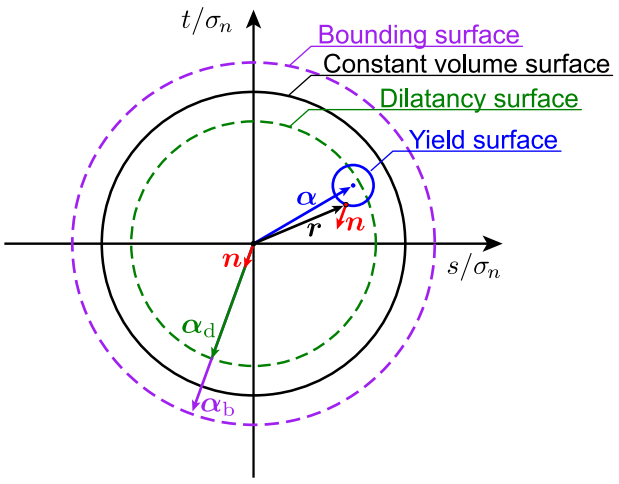

Fig. 3. Characteristic model surfaces on a normalised shear plane.

A schematic of the three characteristic surfaces, namely the bounding, dilatancy and constant volume surfaces, and a yield surface, which are used to describe the constitutive formulations in the subsequent sections, is illustrated on a normalised shear plane in Fig. 3. Even though the circular shapes of the characteristic and yield surfaces on the normalised shear plane (or conical in local stress space) suggests Lode angle independency, their resultant global counterparts produced by the multilaminate framework intrinsically exhibit Lode angle dependency, resembling a smoothed approximation to the Mohr–Coulomb failure surface, particularly for the selected number of sampling planes. An illustrative example showing the shape of the resultant global yield surface can be found in Bayraktaroglu et al. (2023).

2.2. Fabric anisotropy

In this section, an outline of a multilaminate-specific ACST is presented in three stages. In the first stage, the initial microstructure of a soil is idealised using a contact normal-based cross-anisotropic deviatoric fabric tensor:

$$\boldsymbol{F}_{\mathrm{glob}} = F_{\mathrm{norm}} \begin{bmatrix} \frac{-1}{\sqrt{6}} & 0 & 0 \\ 0 & \frac{2}{\sqrt{6}} & 0 \\ 0 & 0 & \frac{-1}{\sqrt{6}} \end{bmatrix} \tag{2}$$

where F_{norm} is an input parameter used to define the norm of the global deviatoric fabric tensor $\boldsymbol{F}_{\mathrm{glob}}$ and the unit-norm bracketed term defines the orientation of the fabric, with, in this case, its major principle direction selected to be in the y-direction. It is worth noting that $\boldsymbol{F}_{\mathrm{glob}}$ is a fabric tensor normalised by its critical state norm to ensure that F_{norm} attains unity at the critical state, i.e. $F_{\mathrm{norm}} = F^*_{\mathrm{norm}}/F^*_{\mathrm{crit.}}$, where * indicates the non-normalised counterpart; further details can be found in Dafalias (2016) and Wang et al. (2020b). From a physical standpoint, during the deposition/pluviation process the long axis of particles tends to align perpendicular to the deposition direction, which results in the major principle fabric direction being concentrated in the deposition direction. Additional information regarding the physical description, sign and magnitude of F_{norm} can be found in Bayraktaroglu et al. (2023). Following the description of $\boldsymbol{F}_{\mathrm{glob}}$, prior to shearing the fabric vectors at each sampling plane are calculated as

$$\boldsymbol{F} = N_{\mathrm{sp}}\, w_i \begin{pmatrix} (\boldsymbol{F}_{\mathrm{glob}}\boldsymbol{n}_i)\,\boldsymbol{n}_i \\ (\boldsymbol{F}_{\mathrm{glob}}\boldsymbol{n}_i)\,\boldsymbol{n}_s \\ (\boldsymbol{F}_{\mathrm{glob}}\boldsymbol{n}_i)\,\boldsymbol{n}_t \end{pmatrix} \tag{3}$$

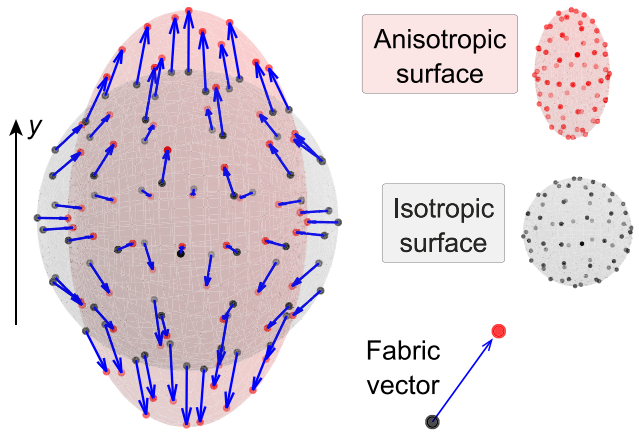

Fig. 4. Discretisation of contact normal distributions using fabric vectors.

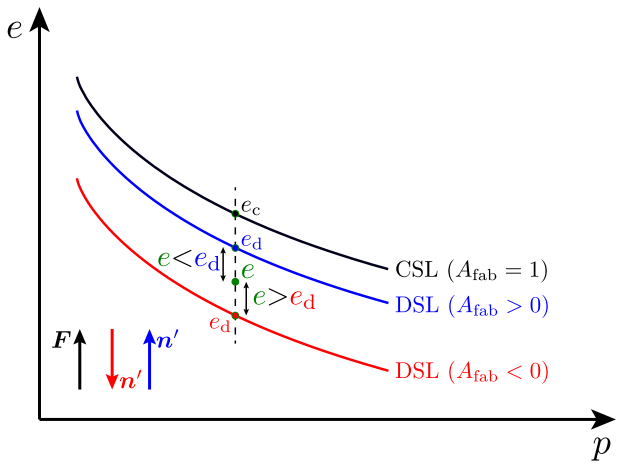

Fig. 5. Illustration of the fabric dependence of DSL.

Here, the fabric vector $\boldsymbol{F}$ is used to quantify the influence of $\boldsymbol{F}_{\text{glob}}$ on the behaviour of the ith sampling plane. The terms N_{sp} and w_i originate from the discretisation of the unit sphere into a finite number of sampling planes. N_{sp} denotes the total number of sampling planes, while the coefficient w_i is the numerical integration weight of the corresponding sampling plane, which ensures that the discrete summation over all planes is consistent with the continuous integration over the unit sphere. A detailed description of integration weights is provided in Lebedev (1976), and the specific values used in the present multilaminate framework with 33 × 2 sampling planes can be found in Bažant and Oh (1986).

In Fig. 4, the contact normal distributions of initially isotropic ($F_{\text{norm}} = 0$) and anisotropic ($F_{\text{norm}} > 0$) sands are visualised using a sphere and an ellipse, respectively. While the spherical shape indicates that the contact normals are distributed without any directional bias, the distorted ellipse shows that the majority of the contact normals are aligned in the vertical direction. In this paper, this distortion representing the tendency of the contact normal directions is incorporated through fabric vectors in Eq. (3), rather than a fabric tensor.

In the second stage, at each sampling plane, a scalar-valued fabric anisotropic variable A_{fab} is derived to incorporate fabric effects into the constitutive formulations:

$$A_{\text{fab}} = \boldsymbol{F}\boldsymbol{n}' \tag{4}$$

where $\boldsymbol{n}' = \mathrm{d}\boldsymbol{\varepsilon}^{\text{p}}_{\text{dev}}/|\mathrm{d}\boldsymbol{\varepsilon}^{\text{p}}_{\text{dev}}|$ represents the direction of the local plastic deviatoric strain rate vector $\mathrm{d}\boldsymbol{\varepsilon}^{\text{p}}_{\text{dev}}$. While stress-based formulations for $\boldsymbol{n}'$ such as the one employed in Bayraktaroglu et al. (2023) yield equivalent performance under monotonic loading conditions, they are not appropriate for modelling the cyclic response.

In the third and final stage, a plastic strain driven local fabric evolution rule, modified from Petalas et al. (2020), is defined for the fabric vectors:

$$\mathrm{d}\boldsymbol{F} = k_{\text{fab}} \exp\left(A_{\text{fab}}\right)\left(\boldsymbol{n}' - (1+D)\,\boldsymbol{F}\right)|\mathrm{d}\boldsymbol{\varepsilon}^{\text{p}}_{\text{dev}}| \tag{5}$$

where k_{fab} is a model constant controlling the speed of the evolution and the incorporation of A_{fab} makes it loading direction-dependent. Additionally, the inclusion of the dilatancy D, following Yang et al. (2018), allows $|\boldsymbol{F}|$ to have values larger than 1 for dense sands before reaching the critical state. Although it is possible to formulate a stress-driven fabric evolution rule, such as the one proposed by Wan and Guo (2004), it results in two main undesired consequences: a change in the fabric vector upon elastic unloading, and the omission of intense fabric changes under complex loading conditions such as during stress principal axes rotation (SPAR) at fixed principal stress values and loading reversals under cyclic loading conditions.

To sum up, unlike classical ACST-based models where both A_{fab} and fabric evolution formulations are defined in tensorial space, in this paper their multilaminate counterparts in Eqs. (4) and (5), respectively, are formulated at sampling planes in a vectorial space. This vectorial formulation allows for an independent and unique evolution pattern at each sampling plane, and provides a more accurate representation of the fabric effects and their evolution under complex loading conditions. By departing from traditional tensorial space, the proposed approach may offer improved insights for modelling the anisotropic behaviour of sands.

2.3. Constitutive formulations

In this section, an ACST-based semi-micromechanical bounding surface plasticity model is presented. The aforementioned vectorial fabric formulations are linked to the relevant constitutive formulations to incorporate the fabric effects.

2.3.1. Critical and dilatancy state lines

The ACST is an extension of the well-known CST and accounts for the anisotropic nature of soil. In ACST, the state of the soil is defined using the so-called dilatancy state line (DSL), which is formulated as an anisotropic counterpart of the CSL considering the relative orientation between the fabric and loading directions. In the proposed model, the CSL in void ratio–volumetric normal stress (i.e. e–$\sigma_{n,\text{vol}}$) space is defined using the formulation proposed by Wan and Guo (1998):

$$e_{\text{c}} = e_{\text{c0}} \exp\left(-\left(\frac{\sigma_{n,\text{vol}}}{h_{\text{s}}}\right)^{n}\right) \tag{6}$$

where e_{c0}, h_{s} and n are model input parameters. Following the determination of the CSL, the anisotropic measure of the state of the soil is formulated through the DSL as

$$e_{\text{d}} = e_{\text{c}} + e_{\text{A}}\left(A_{\text{fab}} - 1\right) \tag{7}$$

where the level of downward scaling of the DSL is controlled by the input parameter e_{A} and the fabric anisotropic variable A_{fab}, as illustrated in Fig. 5.

In Fig. 5, the relationship between the fabric vector $\boldsymbol{F}$ and the loading direction vector $\boldsymbol{n}'$ is illustrated, with their influence on the location of the DSL shown for two extreme cases represented by blue and red colours. The blue colour depicts a scenario where the loading direction vector aligns with the fabric vector, resulting in $1 > A_{\text{fab}} > 0$. Conversely, the red colour represents a scenario where the loading direction vector opposes the fabric vector, leading to $A_{\text{fab}} < 0$ and causing the DSL to shift further downward. These two cases are referred to as extreme because, for a given fabric structure, they correspond to cases where the maximum and minimum possible values of A_{fab}

are calculated. Accordingly, the DSLs in these scenarios act as boundaries, and depending on the loading direction, the actual DSL will lie somewhere between these two extremes. In both extreme cases, even though the soil may have the same stress, fabric structure and void ratio (with its location indicated by a green dot in the $e-p$ space), its behaviour differs. While $A_{\text{fab}} > 0$ results in $e < e_{\text{d}}$, indicating a dilative behaviour, $A_{\text{fab}} < 0$ leads to $e > e_{\text{d}}$, indicating a contractive behaviour. Unlike the classical critical state theory, the ACST differentiates these two scenarios based on the loading direction. Such loading orientation-dependent distinct soil responses are commonly observed in triaxial compression and extension tests, as well as in cyclic loading tests.

The local fabric formulations in Eqs. (4) and (5) ensure the uniqueness of the CSL, such that, at a sampling plane towards the critical state, the fabric vector reaches its critical state value, i.e. $\boldsymbol{F} \rightarrow \boldsymbol{F}_{\text{c}} = \boldsymbol{n}'$, and A_{fab} evolves to 1. As a result, the DSL becomes identical to the CSL.

2.3.2. Yield surface

The formulation of the yield surface is adopted from Dafalias and Manzari (2004) as

$$f = [(\boldsymbol{r}-\boldsymbol{\alpha})(\boldsymbol{r}-\boldsymbol{\alpha})]^{1/2} - m \tag{8}$$

where the scalar m defines the size of the elastic core on the normalised shear plane. Recalling the multilaminate adaptation, it is worth noting that the ingredients of Eq. (8), i.e. $\boldsymbol{r}$ and $\boldsymbol{\alpha}$, are vectors rather than tensors.

2.3.3. Elasticity formulation

The elastic part of the model, both at local sampling planes and the global tensorial field, is defined using the hypoelastic formulation proposed by Richart et al. (1970):

$$G = G_0 p_{\text{at}} \frac{(2.97-e)^2}{1+e} \left(\frac{p}{p_{\text{at}}}\right)^{1/2} \tag{9}$$

where the shear modulus constant G_0 is an input parameter and p_{at} is the reference atmospheric pressure.

2.3.4. Characteristic surfaces

The proposed model consists of three concentric surfaces, namely the constant volume, bounding and dilatancy surfaces as illustrated in Fig. 3. Even though the size of the constant volume surface on a normalised shear plane is fixed (i.e., state independent) and determined by the input parameter M, the sizes of the bounding and dilatancy surfaces depend on the state of the sand and the relative orientation between $\boldsymbol{F}$ and $\boldsymbol{n}'$, i.e. A_{fab}. The size of the bounding surface, which determines the peak attainable stress ratio, is defined as

$$\alpha_{\text{b}} = f_{\text{b}} M - m \tag{10}$$

and the size of the dilatancy surface, which defines contractive to dilative behaviours, is formulated as

$$\alpha_{\text{d}} = f_{\text{d}} M - m \tag{11}$$

In Eqs. (10) and (11), the scaling factors f_{b} and f_{d} are formulated as

$$f_{\text{b}} = \left(1+\zeta e_{\text{d}}^{-1}\right)^{-\alpha} = \left(\frac{e}{e_{\text{d}}}\right)^{-\alpha} \tag{12}$$

and

$$f_{\text{d}} = \left(1+\zeta e_{\text{d}}^{-1}\right)^{\beta} = \left(\frac{e}{e_{\text{d}}}\right)^{\beta} \tag{13}$$

where $\zeta = e - e_d$ is the dilatancy state parameter and the exponential constants α and β are input parameters. Following the calculation of the sizes of the characteristic surfaces, corresponding image back-stress ratio vectors can be derived using the loading direction vector, such that $\boldsymbol{\alpha}_{\text{b}} = \alpha_{\text{b}}\boldsymbol{n}$ and $\boldsymbol{\alpha}_{\text{d}} = \alpha_{\text{d}}\boldsymbol{n}$.

2.3.5. Kinematic hardening

The mobilisation of the back-stress ratio vector $\boldsymbol{\alpha}$ is controlled using the kinematic hardening formulation:

$$\mathrm{d}\boldsymbol{\alpha} = \mathrm{d}\lambda h \left(\boldsymbol{\alpha}_{\text{b}} - \boldsymbol{\alpha}\right) \tag{14}$$

where $\mathrm{d}\lambda$ is the plastic multiplier and the hardening coefficient h is adopted from Petalas et al. (2020) as

$$h = \frac{G_0 h_0 \exp\left(k_{\text{h}} A_{\text{fab}}\right)\left(1/e - c_{\text{h}}\right)^2}{\left(\boldsymbol{\alpha}-\boldsymbol{\alpha}_{\text{in}}\right)\boldsymbol{n}} \left(\frac{p_{\text{at}}}{\sigma_n}\right)^{1/2} \tag{15}$$

where h_0, k_{h} and c_{h} are material constants. The fabric parameter k_{h} scales the influence of the fabric on the plastic hardening modulus, and is initially set to a default value of 1.0. Within the semifluidised zone, k_{h} evolves towards 0, effectively eliminating the fabric's influence on the hardening response. This evolution reflects the physical observation that the influence of initial fabric anisotropy is progressively "wiped out" during liquefaction, as the semifluidisation process disrupts the original particle contact network. Such behaviour is consistent with DEM findings, which show that in the post-liquefaction stage, fabrics of all samples converge to the same anisotropic state within a few loading cycles, with the fabric direction aligning coaxially with the principal stress direction, irrespective of the initial fabric configuration (Wei and Wang, 2016). The initial back-stress ratio $\boldsymbol{\alpha}_{\text{in}}$ is equal to the back-stress ratio $\boldsymbol{\alpha}$ at the initiation of a new loading process, which is detected whenever $\left(\boldsymbol{\alpha}-\boldsymbol{\alpha}_{\text{in}}\right)\boldsymbol{n} < 0$. Note that, during small unloading–reloading events, which are commonly observed under dynamic loading conditions, the denominator of Eq. (15) may yield $\left(\boldsymbol{\alpha}-\boldsymbol{\alpha}_{\text{in}}\right)\boldsymbol{n} = 0$, resulting in an unrealistically stiff response commonly referred to as stress overshooting (Dafalias, 1986; Dafalias and Taiebat, 2016). In this paper, simulations of regular cyclic laboratory tests with relatively large stress/strain amplitudes require no overshooting correction.

2.3.6. Flow rule and dilatancy formulation

The direction of the plastic flow at each sampling plane is calculated by using a non-associative flow rule. While the plastic flow in the shear direction is determined using the normality rule applied to the yield function, the plastic flow in the normal direction to the sampling planes is governed by the stress-dilatancy formulation given by

$$D = k_{\text{d}} A_{\text{d}} \left(\boldsymbol{\alpha}_{\text{d}} - \boldsymbol{\alpha}\right)\boldsymbol{n} \tag{16}$$

Note that the local associativeness in the shear direction does not yield deviatoric associativeness in global stress space.

During the undrained cyclic shearing of dense sands, the use of Eq. (16) with a constant/fixed A_{d} beyond the phase transformation line (PTL) results in a termination of the progressive reduction of the mean effective stress far from the zero mean effective stress. Consequently, this approach fails to capture the cyclic mobility response and the formation of the well-known butterfly-shaped stress path. To address this undesired response, the evolving A_{d} formulation proposed by Dafalias and Manzari (2004) is adopted:

$$A_{\text{d}} = A_0 \left(1 + \langle \boldsymbol{z}\boldsymbol{n}\rangle\right) \tag{17}$$

with

$$\mathrm{d}\boldsymbol{z} = -c_{\text{z}}\langle -\mathrm{d}\varepsilon_n^{\text{p}}\rangle \left(z_{\max}\boldsymbol{n} + \boldsymbol{z}\right) \tag{18}$$

where A_0, c_{z} and $z_{\max}$ are model input parameters. The Macaulay brackets $\langle\ \rangle$ ensure that the fabric dilatancy vector $\boldsymbol{z}$ evolves during dilation only. Even though the structure of Eqs. (17) and (18) looks similar to the one proposed by Dafalias and Manzari (2004), they are downscaled to the vectorial field to enable the proposed framework to yield independently evolving dilatancy responses at each sampling plane.

Finally, the variable k_{d} is introduced to capture the changing dilative response of sands during unloading/reloading events. Inspired by Cheng and Detournay (2021), k_{d} is formulated as

$$k_{\mathrm{d}} = 1 + \frac{\langle |\boldsymbol{\alpha}_{\mathrm{hmax}}| - |\boldsymbol{\alpha}| \rangle}{|\boldsymbol{\alpha}_{\mathrm{hmax}}| - |\boldsymbol{\alpha}|} \left(k_{\mathrm{dila}} \left(\boldsymbol{\alpha} - \boldsymbol{\alpha}_{\mathrm{in}} \right) \boldsymbol{n} - 1 \right) \tag{19}$$

where k_{dila} is an input parameter, and the Macaulay brackets $\langle\ \rangle$ ensure that k_d is equal to 1.0 during virgin loading and $k_{\mathrm{dila}} \left(\boldsymbol{\alpha} - \boldsymbol{\alpha}_{\mathrm{in}} \right) \boldsymbol{n}$ during unloading/reloading. In Eq. (19), the state parameter $\boldsymbol{\alpha}_{\mathrm{hmax}}$ represents the historic maximum back-stress ratio (i.e. memory) surface. This approach enables differentiation of the soil's dilative response between virgin loading and subsequent loading reversals. The parameter k_{dila} can also be linked to the relative density D_{r}, allowing the model to account for the influence of density on dilatancy, in a manner similar to that proposed by Cheng and Detournay (2021). In this paper, even though there is no shrinkage algorithm defined for the memory surface, it is assumed to vanish (i.e., $|\boldsymbol{\alpha}_{\mathrm{hmax}}| \rightarrow 0.0$ and $k_{\mathrm{dila}} \rightarrow 1.0$) upon entering the semifluidised zone.

2.4. Semifluidised state

Up to this section, an anisotropic cyclic multilaminate constitutive model has been formulated for sands. Nonetheless, the simulation results of post-liquefaction behaviour reveal significant inconsistencies with respect to experimental observations. Specifically, the proposed model exhibits biased and repetitive deviatoric strain increments, as it fails to adequately account for the progressive reduction of plastic stiffness and dilatancy within the solid to fluid-like transition, i.e. semifluidised, zone. In this section, in order to enhance the prediction capabilities of the model at low mean effective stresses, the semifluidised state theory proposed by Barrero et al. (2020) has been adopted. The degradation of an arbitrary model variable k at a sampling plane is formulated as

$$k_{\mathrm{sf}} = k[\left(1 - \langle 1 - \sigma_n/\sigma_{\mathrm{th}} \rangle\right)^{x\ell} + f_\ell] \tag{20}$$

where x is a model input parameter, and f_ℓ is a constant with a default value of 0.01 preventing k_{sf} from evolving to zero. The threshold normal stress σ_{th}, which is set to a default value of 10 kPa, determines the size of the semifluidised zone. The rate of the ever-increasing state variable, namely the strain liquefaction factor ℓ, has been introduced as

$$\mathrm{d}\ell = \mathrm{d}\lambda[c_\ell \langle 1 - \sigma_n/\sigma_{\mathrm{th}} \rangle (1 - \ell)^{n_\ell}] - c_{\mathrm{r}} \ell |\mathrm{d}\epsilon_n^{\mathrm{p}}| \tag{21}$$

where c_ℓ and c_{r} are model constants controlling the dependency of the evolution rate on the plastic shear and normal strains, respectively, and n_ℓ is a constant with a default value of 8.0. In Eqs. (20) and (21), $\langle 1 - \sigma_n/\sigma_{\mathrm{th}} \rangle$ ensures that both the degradation and the evolution of ℓ take place only within the semifluidised zone, i.e. while $\sigma_n < \sigma_{\mathrm{th}}$. Note that all the default semifluidised model constants are adopted from the work of Barrero et al. (2020) and c_{r} is set to 0.0 while examining the undrained response of sands.

In this paper, in order to provide the aforementioned fluid-like behaviour at low-stress ranges, i.e. low shear resistance and dilatancy, the h_0 and A_0 values in Eqs. (15) and (17) are degraded using Eq. (20). A comparison of the proposed model with and without the incorporation of the semifluidised state theory is presented in Fig. 6.

In Fig. 6, the undrained cyclic triaxial test simulations show that the incorporation of the semifluidised state theory significantly improves the post-liquefaction response of the model. As intended, employing Eq. (20) results in progressively increasing plastic shear strain amplitudes upon liquefaction. Note that, since the mobilisation of ℓ takes place within the semifluidised zone, no change in the response is observed during the pre-liquefaction phase. This simplifies the calibration of the model, because the semifluidised state parameters do not interfere with or modify the pre-liquefaction response of the sand.

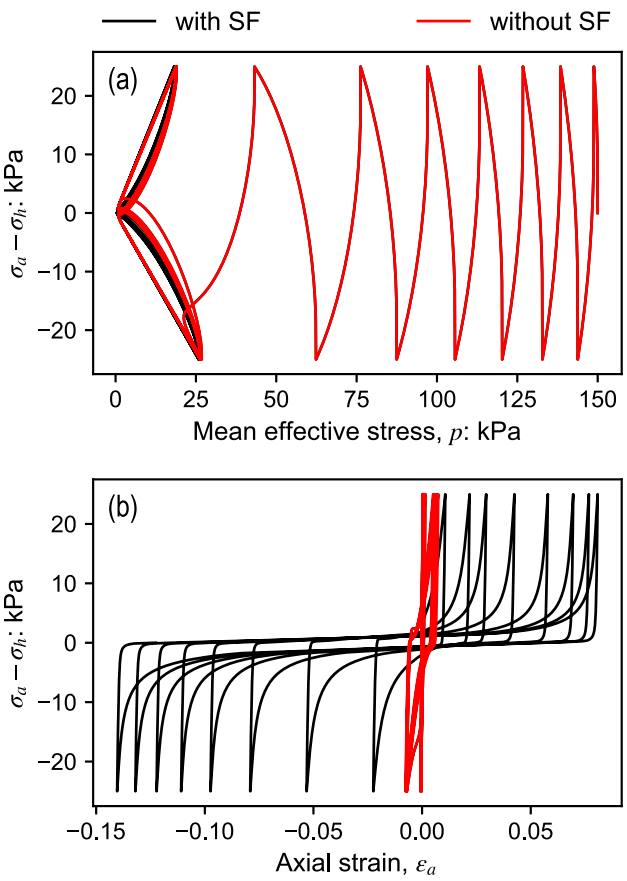

Fig. 6. Influence of the incorporation of the semifluidised state theory on undrained cyclic triaxial test simulations.

It is important to acknowledge that the semifluidised state theory does not guarantee the non-biased plastic strain accumulations observed in Fig. 6. The anisotropic failure surfaces which are employed by advanced constitutive models to capture the resultant stress ratios for changing loading directions may cause the generated stress–strain loops to be shifted to one side during cyclic loading. These unrealistic predictions of the plastic strain accumulations are generally referred to in the literature as biased plastic strain accumulations and are commonly observed in cyclic triaxial test simulations where the stress path travels through compression and extension directions resulting in always greater strain accumulation on the extension side. In order to eliminate this, Liao et al. (2022) employed a Lode angle independent formulation. However, this approach causes two main undesired outcomes: firstly, upon reaching cyclic mobility, symmetric butterfly stress-paths are formed, and secondly, unconditionally symmetric stress–strain loops are generated. Both of these features are inconsistent with experimental observations. Recently, Liu et al. (2020) proposed a modified dilatancy formulation controlling the aforementioned shifting and Yang et al. (2022a) employed a similar approach within the semifluidised state theory.

In this work, the modification proposed by Yang et al. (2022a) has been adopted to capture both the varying stress ratios over changing loading directions and the non-biased plastic strain accumulations, such that the hardening and dilatancy formulations in Eqs. (15) and (16), respectively, are modified as

$$h' = hg(\beta)^{n_{\mathrm{g}}} \tag{22}$$

and

$$D' = Dg(\beta)^{n_{\mathrm{g}}} \tag{23}$$

where n_g is an input parameter controlling the non-biased plastic strain accumulations, and β is equivalent to the Lode angle at the sampling plane and defines the directions of the stress paths followed in differently oriented sampling planes. The local interpolation function $g(\beta)$ is defined as

$$g(\beta) = 1 - \frac{\sigma_{n,dev}}{\sigma_n} \tag{24}$$

3. Calibration

The proposed model requires the calibration of 21 parameters, whose descriptions and values used for Toyoura sand in the current simulations are listed in Table 1. Several of the model parameters, namely G_0, υ, m, h_0, c_h, A_0, c_z and z_{max} are inherited from the reference model SANISAND04 and their calibration procedures can be found in Dafalias and Manzari (2004) and Taiebat and Dafalias (2008). The critical state parameters are all physical parameters: e_{c0}, h_s and n are used to define the CSL in e–p space, and require tests at large shear strain in which the soil reaches the critical state. While the cyclic dilatancy parameter k_{dila} is originally formulated as a function of relative density in Cheng and Detournay (2021), in this paper cyclic experimental data are employed for its calibration. As previously stated, the constant volume stress ratio M differs from its Lode angle-dependent global counterpart, i.e. the critical state stress ratio. For the determination of M, the critical state stress ratio in a triaxial compression test can be used. The exponential parameters α and β can be back-calculated from peak friction and phase transformation angles, respectively, as described in Wan and Guo (1999). The calibration of the fabric parameters requires granular level studies, which rarely exist, so that model users will mostly have to determine parameter values through performing trial-and-error calculations. Note that this type of trial-and-error-based fabric tensor calibration requires an extensive data set, including different modes of shearing. However, locating the phase transformation lines using triaxial compression and extension test results may help to decrease the number of trial runs, since e_A and F_{norm} together locate the DSL in e–p space as described in Petalas et al. (2020). Even though F_{norm} is a material property and inherent fabric characteristics modulate its limit values, it strongly depends on factors such as sample preparation method and loading history. Finally, the semifluidised state parameters are calibrated through parametric sensitivity analyses, as described by Barrero et al. (2020) and Yang et al. (2022a). Unlike the reference model, in semifluidised state theory-based models, relatively large fabric dilatancy parameters c_z and z_{max} are employed to facilitate the formation of a locked up butterfly shape upon a loading reversal following dilative deformation. This approach prevents potential bias in the plastic strain accumulations while approaching the semifluidised state.

Table 1
Model parameters for Toyoura sand.

Category	Parameter	Value
Elasticity	G_0	125
	υ	0.18
Critical state	M	1.25
	h_s	20 000
	n	0.74
	e_{c0}	0.934
Yield surface	m	0.017
Plastic modulus	h_0	7.5
	c_h	0.93
	α	1.0
Dilatancy	A_0	0.704
	k_{dila}	2.5
	β	2.8
	z_{max}	25.0
	c_z	2000
Fabric anisotropy	e_A	0.06
	F_{norm}	0.55
	k_{fab}	8.0
Semifluidised state	c_{ℓ}	65
	x	4.4
	n_g	1.1

4. Model performance

In this section, the model's capabilities under undrained loading conditions are demonstrated by simulating a set of experimental data for Toyoura sand.

4.1. Monotonic tests

Even though the present work focuses on the undrained cyclic behaviour of Toyoura sand, a series of monotonic triaxial compression and extension test simulations are presented to show that the set of parameters listed in Table 1 is not exclusively calibrated for simulating the cyclic response of the sand. In addition, these tests provide a valuable opportunity to observe extreme fabric and loading configurations, which are important for calibrating the fabric parameters.

In Fig. 7, specimens with similar initial relative densities and fabric characteristics have been sheared in triaxial compression and extension tests under different confining stresses. The significant fabric anisotropy induced changes, observed in the experiments, are adequately captured using the proposed model. In Fig. 7(e), the two extreme locations of the dilatancy state line (DSL) are presented, with their locations at each sampling plane bounded by the red and blue lines according to the relative orientation of the loading direction vector with respect to the fabric vector. Furthermore, the influence of incorporating A_{fab} into the fabric evolution formulation in Eq. (5) is clearly illustrated in Fig. 7(d), which allows the model to reproduce the rapid fabric mobilisation observed in triaxial compression and the comparatively slower mobilisation seen in triaxial extension. A more detailed explanation of these two extreme cases can be found in Fig. 5, where the influence of the loading direction vectors on the DSL location is discussed further.

In addition to the undrained simulations, six drained experiments conducted by Verdugo and Ishihara (1996) under two different consolidation pressures (100 kPa and 500 kPa) and various initial void ratios are compared with the corresponding simulations in Fig. 8. The volumetric changes are shown to be adequately captured by the model.

4.2. Cyclic tests

4.2.1. Cyclic undrained triaxial tests

The first cyclic simulation is performed for a cyclic undrained triaxial test on Toyoura sand carried out by Yamada et al. (2010). The isotropically consolidated specimen, under a confining pressure of 98.1 kPa, is sheared with a deviatoric stress amplitude of q^{amp} = 39.2 kPa.

The comparisons presented in Fig. 9 show that the simulation results generated by the proposed model demonstrate a satisfactory agreement with the experimental data in both the pre- and post-liquefaction phases. While the incorporation of the semifluidised state theory enables reproduction of the fluid-like behaviour characterised by low shear resistance and large plastic shear strains, the modifications introduced in Eqs. (22) and (23) enable the model to produce non-biased plastic strain accumulations while preserving the Lode angle dependency.

To further evaluate the performance of the model, an additional cyclic undrained triaxial simulation was conducted based on the test reported by Koseki et al. (2016). In this case, a specimen with a lower relative density (D_r = 70%) and subjected to a higher deviatoric stress amplitude (q^{amp} = 80 kPa) was considered. This simulation was used to assess the model's ability to capture the combined effects of relative density and loading amplitude on the cyclic response. The comparisons,

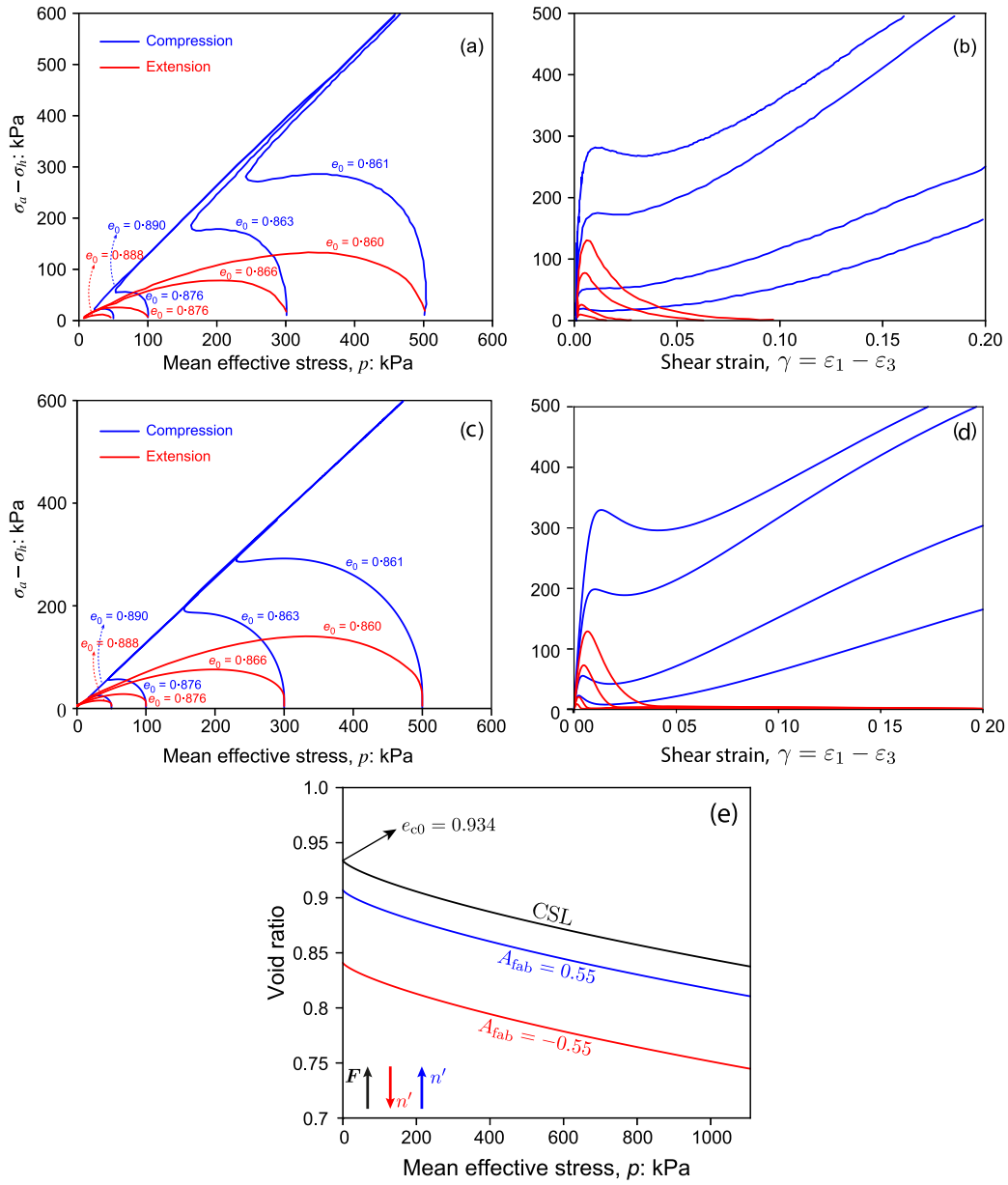

Fig. 7. Comparison of experimental data (a, b) and model response (c, d, e) for undrained triaxial compression and extension tests; data after Yoshimine et al. (1998).

presented in Fig. 10, indicate that the experimental behaviour is satisfactorily reproduced in both the pre- and post-liquefaction phases. In particular, the number of cycles to liquefaction, the accumulation of plastic strains, and the evolution of excess pore water pressure are captured with good accuracy.

4.2.2. Cyclic constant-p triaxial tests

Cyclic constant-p triaxial tests were simulated to evaluate the model performance under more complex loading conditions. The test, carried out by Pradhan et al. (1989), involved a soil specimen with an initial void ratio of 0.845 subjected to cyclic loading under a constant mean effective stress of 98 kPa. This stress path is more demanding than that of conventional undrained cyclic triaxial tests. The comparisons between the experimental data and the corresponding model simulations are presented in Fig. 11.

In Fig. 11, the solid red lines correspond to simulations obtained using the input parameters defined in Table 1, while the dashed lines represent results obtained with the same set of parameters except for $c_z = 4$ and $z_{max} = 600$. One drawback of the semifluidised state formulation is that achieving a locked-up butterfly shape near the apex necessitates relatively large c_z and z_{max} values. This requirement helps, though does not fully ensure, unbiased plastic strain accumulation. However, it also leads to a major limitation: in the drained simulation, large volumetric strains develop upon a loading reversal following dilative deformation. The dashed-line simulation illustrates this effect, highlighting the consequences of using large c_z and z_{max} values.

4.2.3. Cyclic undrained torsional tests

The final set of cyclic simulations is performed for undrained cyclic torsional shear tests on Toyoura sand, as carried out by Zhang (1997). The isotropically consolidated specimens, under a confining pressure of 100 kPa, with relative densities of $D_r = 48\%$ and $D_r = 60\%$, are sheared with a cyclic shear stress amplitude of $\tau^{amp} = 25$ kPa. In these torsional shear tests, the major principal stress direction alternates between ±45° relative to the specimen's vertical axis.

The symmetric stress–strain loops observed in the experiments, in Figs. 12(b) and 13(b), are adequately captured by the model simulations in Figs. 12(d) and 13(d). It is well known that the number of cycles

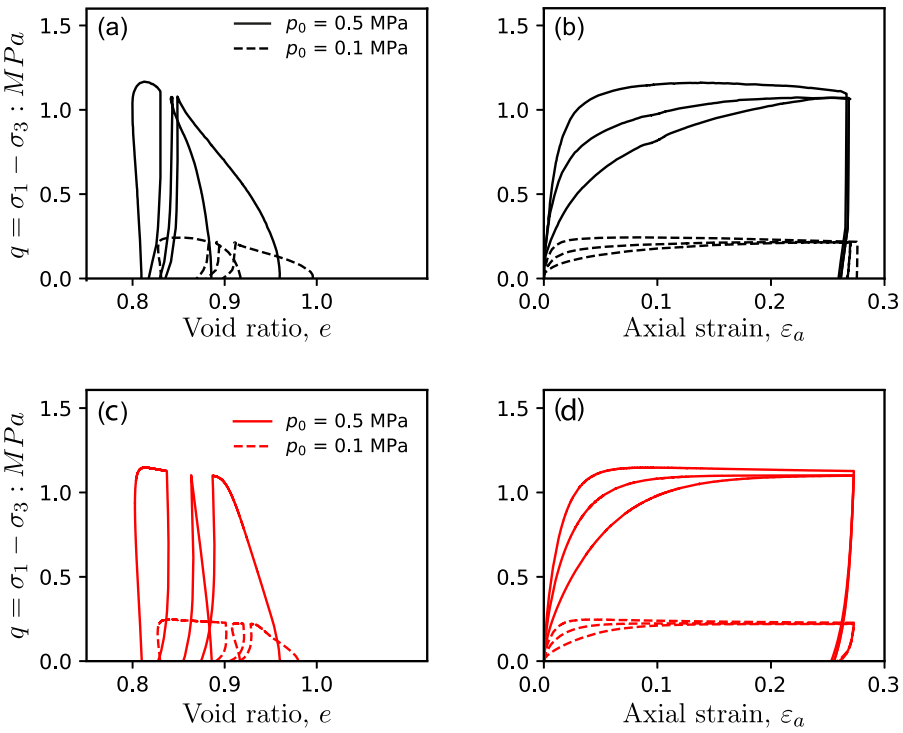

Fig. 8. Comparison of experimental data (a, b) and model response (c, d) for drained triaxial tests; data after Verdugo and Ishihara (1996).

required for the sample to reach liquefaction increases with increasing relative density as observed in Figs. 12(a) and 13(a), which is also well predicted with the proposed model in Figs. 12(c) and 13(c).

Owing to the incorporation of the fabric dilatancy formulation in Eq. (18), the proposed model can reproduce the butterfly-shaped effective stress paths at approximately zero ultimate effective stresses. Once the effective mean stress approaches zero, the semifluidised state is activated; hence, the shear modulus is reduced, resulting in a large shear deformation and a flow liquefaction-like response. However, during the subsequent dilative phase, when the stress goes beyond the semifluidised zone, there is considerable strain hardening and a regain in shear strength. With an increase in ℓ, the simulated deviatoric strain progressively accumulates on both the compression and extension sides during each loading cycle. As a result, the model can satisfactorily simulate the experimental features described above.

Finally, it is important to note that, despite the continued evolution of the fabric structure during the post-liquefaction phase, the influence of fabric on sand behaviour becomes negligible as the mean effective stress approaches zero, due to the decreased contact forces. It is important to recall that the methodology followed in this paper involves deriving a fabric anisotropic variable called A_{fab} using fabric vectors and loading directions, which is then incorporated into relevant constitutive formulations. Specifically, these formulations refer to the plastic hardening modulus and dilatancy formulations in Eqs. (15) and (16), respectively, which are also the equations whose values are degraded through Eq. (20) within the semifluidised zone. In other words, employing the semifluidised state concept directly reduces the dilatancy and plastic hardening modulus, indirectly diminishing the influence of fabric within the semifluidised zone.

5. Conclusions

The anisotropic multilaminate framework proposed by Bayraktaroglu et al. (2023) has been enhanced to reproduce key characteristics of the undrained cyclic response of sands. It has been substantially improved by (1) incorporating a bounding surface plasticity framework, replacing the accumulated plastic strain-based hardening formulation with an incremental plasticity-based hardening formulation; (2) employing a local shear stress decomposition rule to detect loading reversals; (3) enhancing the fabric evolution rule to handle changing fabric structure upon loading reversals; (4) incorporating the semifluidised theory to capture the post-liquefaction response of sands. The outcome of this work provides insights into a new way of handling anisotropy.

The performance of the proposed model has been verified through the simulation of laboratory data for Toyoura sand. The comparisons between the model response and published experimental data show that the proposed constitutive framework is well able to simulate the anisotropic cyclic response of sands. However, incorporating fabric effects into constitutive models for cyclic behaviour remains a challenging task, and further research is needed to develop more comprehensive fabric evolution rules that accurately capture the complex evolutions in fabric structure under cyclic loading conditions. Furthermore, together with the updated dilatancy formulation in Eq. (16), unlike the reference model SANISAND04, the proposed model is expected to yield a better performance while simulating the response of dense sands with low cyclic shear stress ratios, in which the rate of pore pressure accumulation in the experimental tests decreases first and then increases during the pre-liquefaction stage. However, the model's predictions for dense sands could be further enhanced by incorporating a dynamically evolving memory surface similar to the one employed by Liu et al. (2020) and Yang et al. (2022a).

Finally, even though many semi- or micro-mechanical constitutive models are available, most of them require significant computational effort. Even though computational efficiency is not the main concern when performing computationally less demanding element test simulations, they often pose challenges when implemented in finite element models for large-scale geotechnical analyses. To address this concern, the finite element implementation of the proposed model has employed integration point level parallelisation and a stable work scheduling algorithm, resulting in enhanced computational performance of the code. These computational optimisations ensure that the proposed model can be effectively utilised for simulating practical geotechnical problems while maintaining reasonable computational demands.

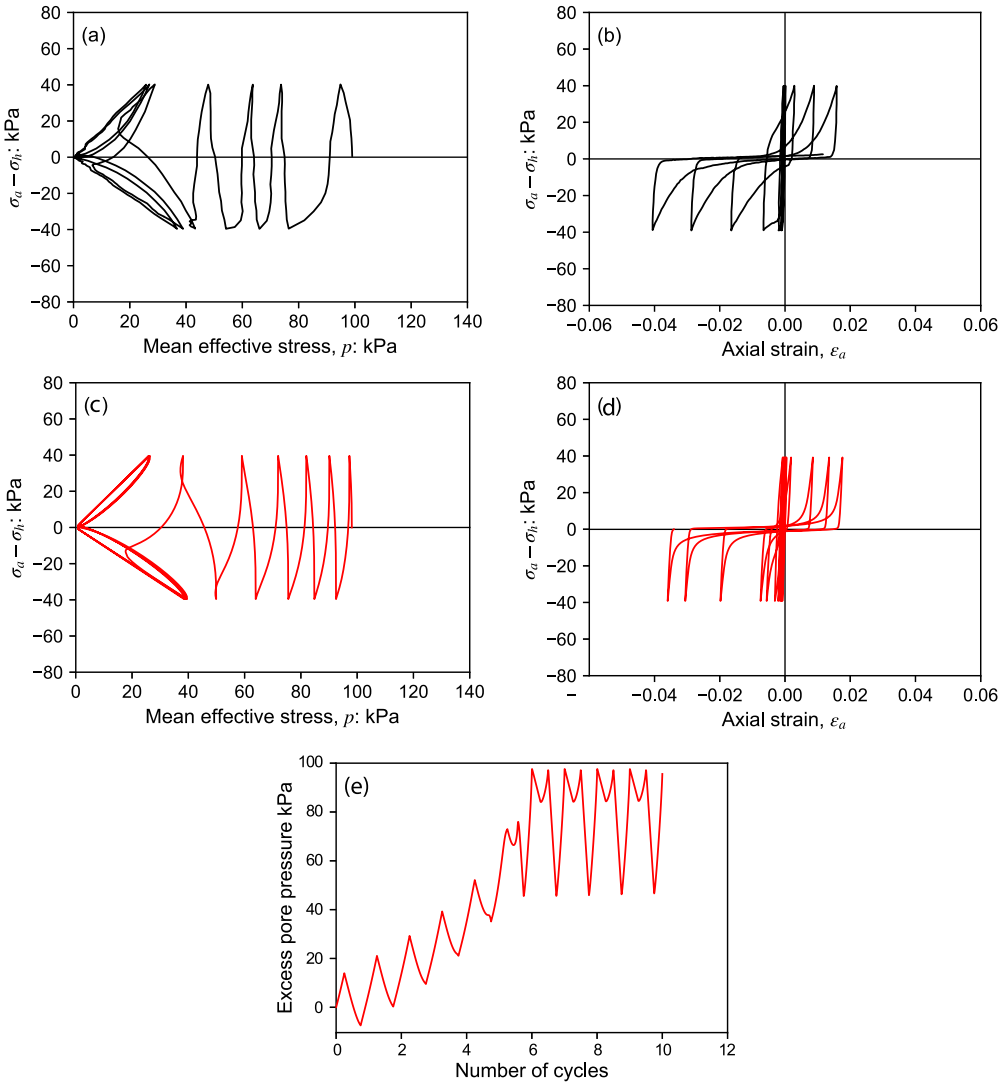

Fig. 9. Comparison of experimental data (a, b) and model response (c, d, e) for undrained cyclic triaxial test ($D_r = 77.1\%$); data after Yamada et al. (2010).

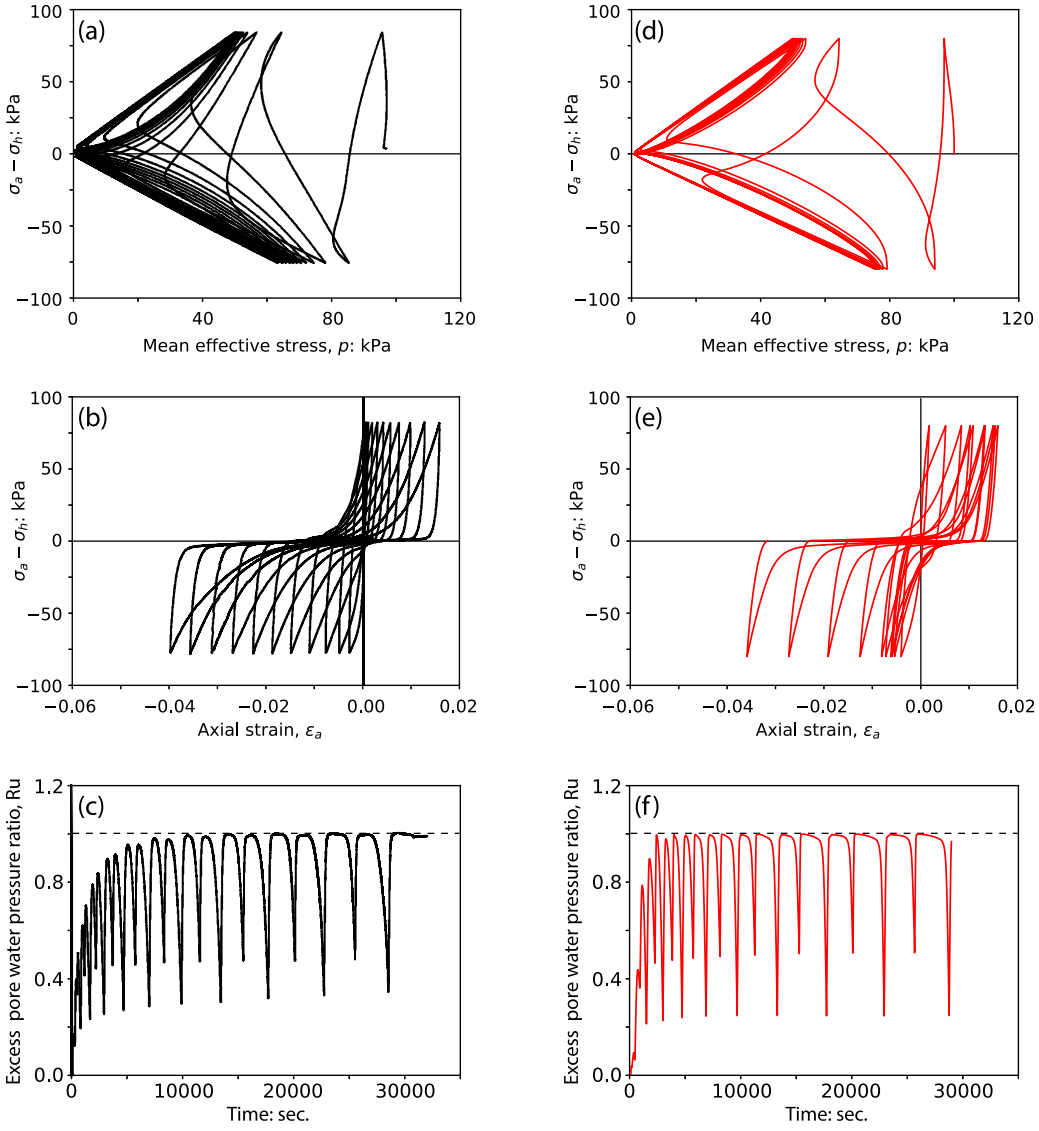

Fig. 10. Comparison of experimental data (a, b, c) and model response (d, e, f) for undrained cyclic triaxial test ($D_r = 70.0\%$); data after Koseki et al. (2016).

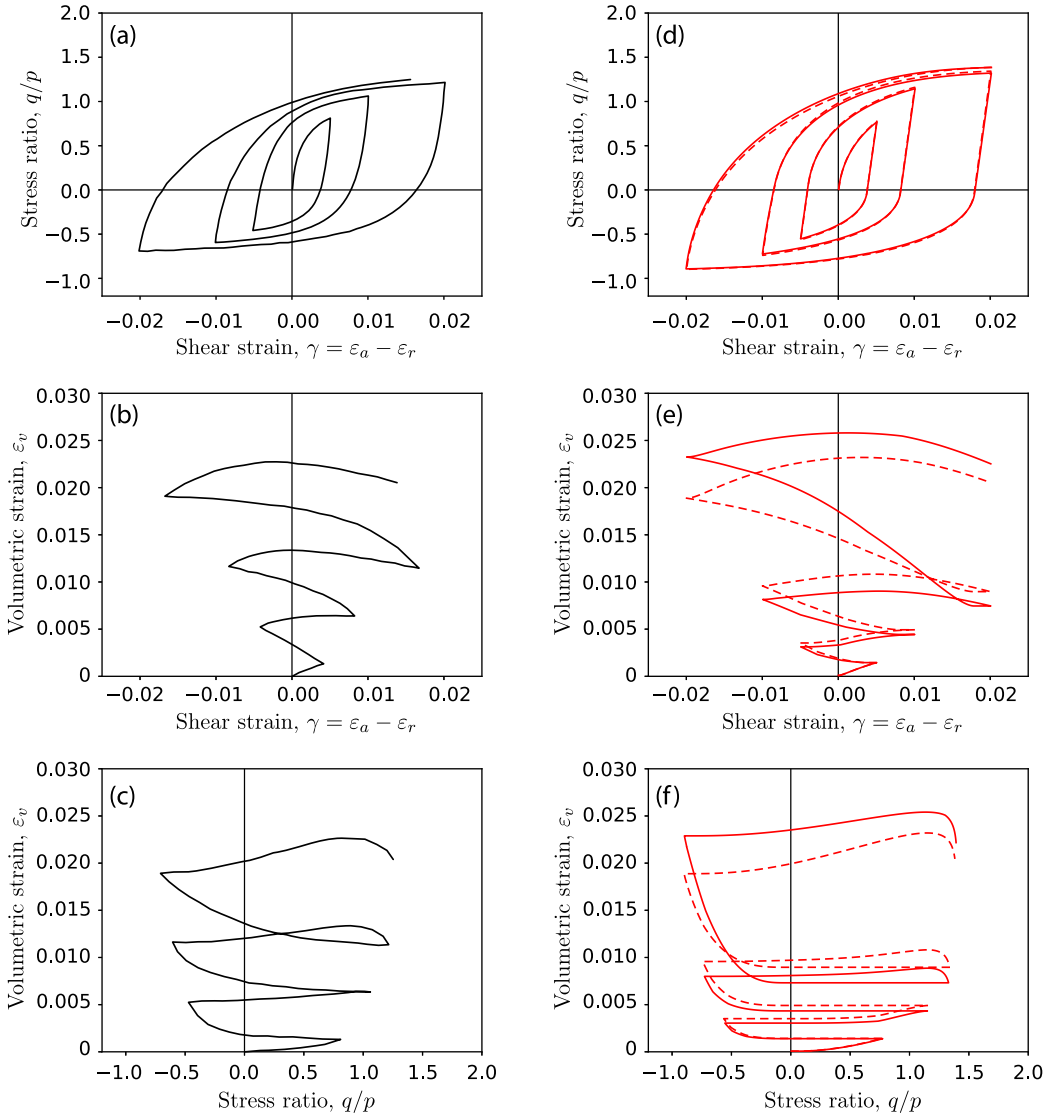

Fig. 11. Comparison of experimental data (a, b, c) and model response (d, e, f) for constant-p triaxial test ($e = 0.845$); data after Pradhan et al. (1989).

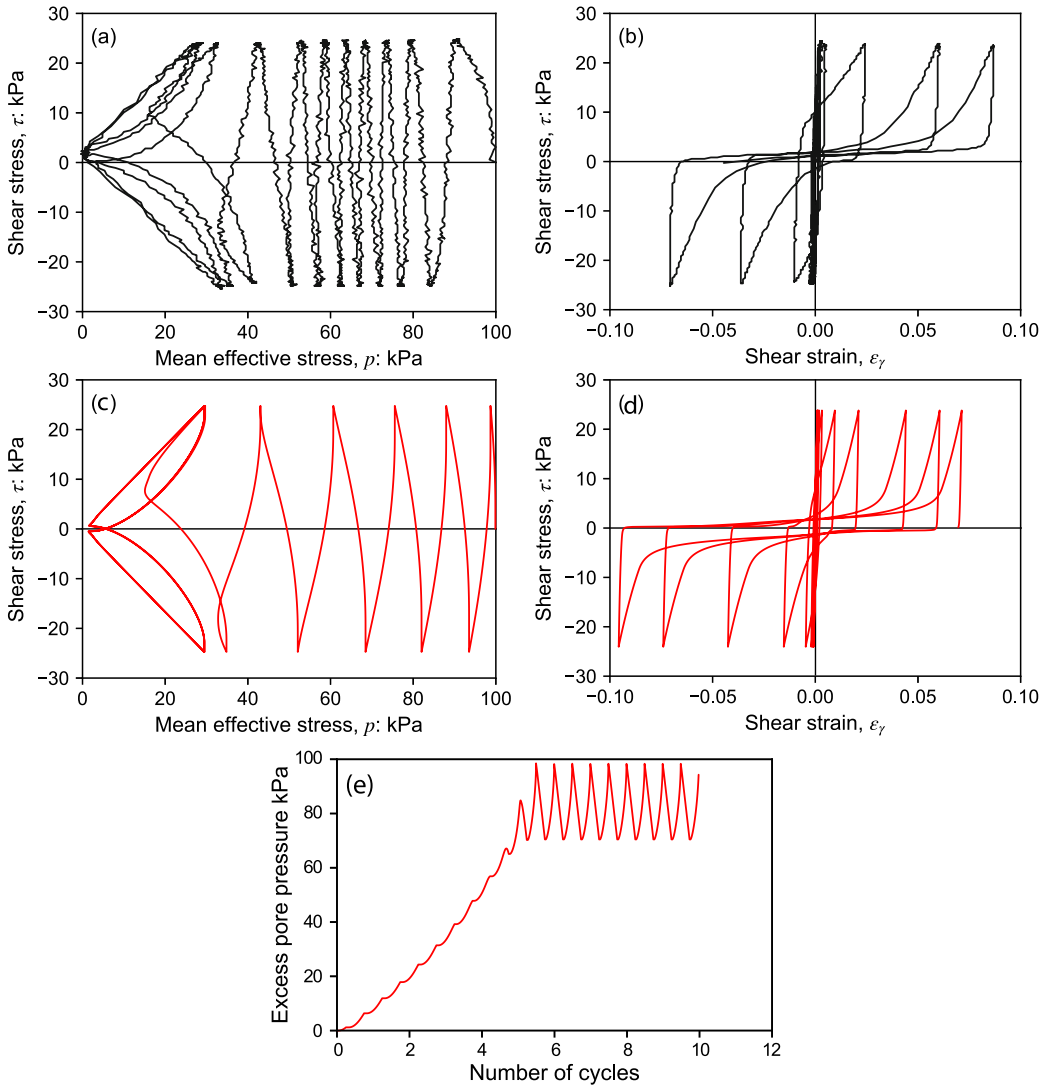

Fig. 12. Comparison of experimental data (a, b) and model response (c, d, e) for undrained cyclic torsional shear test ($D_r = 48.0\%$); data after Zhang (1997).

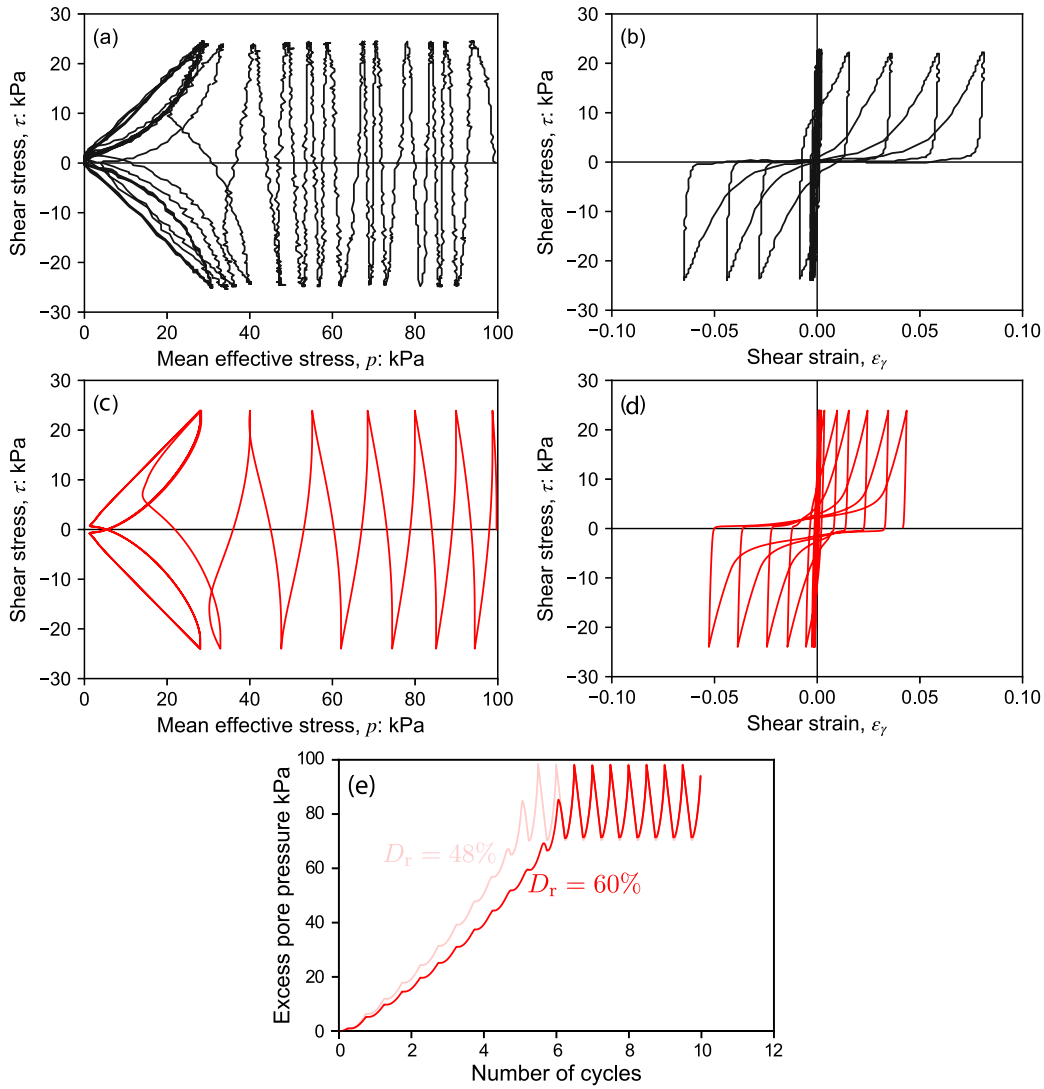

Fig. 13. Comparison of experimental data (a, b) and model response (c, d, e) for undrained cyclic torsional shear test ($D_r = 60.0\%$); data after Zhang (1997).

Notation

A_0	Dilatancy model constant
A_{fab}	Local fabric anisotropic variable (FAV)
c_h	Plastic modulus model constant
c_ℓ	Semifluidised state model constant
c_z	Dilatancy model constant
D	Dilatancy
e	Void ratio
e_A	Fabric model constant, determines the deviation of the dilatancy state line (DSL) from the critical state line (CSL)
e_c	Critical state void ratio
e_{c0}	Critical state void ratio at zero stress
e_d	Dilatancy void ratio (anisotropic measure of e_c)
$\boldsymbol{F}$	Local fabric vector
$\boldsymbol{F}_{glob}$	Global fabric tensor
F_{norm}	Euclidean norm of $\boldsymbol{F}_{glob}$
f	Yield function
f_l	Semifluidised state model constant with a default value of 0.01
G	Hypoelasticity shear modulus
G_0	Hypoelasticity model constant
h	Hardening coefficient for kinematic hardening
h_s	Critical state line model constant
h_0	Hardening coefficient model constant
k_{dila}	Cyclic dilatancy model constant
k_{fab}	Fabric evolution rate model constant
k_h	Fabric hardening coefficient model constant
ℓ	Strain liquefaction factor
M	Constant volume stress ratio
m	Yield surface size model constant
$\boldsymbol{n}$	Unit loading direction vector
n	Critical state line model constant
$\boldsymbol{n}'$	Unit deviator loading vector
n_g	Semifluidised state model constant
$\boldsymbol{n}_i$	Unit normal (or direction cosine) vector of the ith sampling plane
n_ℓ	Semifluidised state model constant with a default value of 8.0
$\boldsymbol{n}_s$	Local unit vector in direction of s
$\boldsymbol{n}_t$	Local unit vector in direction of t
p	Mean effective stress
p_{at}	Atmospheric pressure
$\boldsymbol{r}$	Stress ratio vector

s	Magnitude of shear stress component of $\boldsymbol{\sigma}_i$ along the direction of $\boldsymbol{n}_s$
t	Magnitude of shear stress component of $\boldsymbol{\sigma}_i$ along the direction of $\boldsymbol{n}_t$
x	Semifluidised state model constant
$\boldsymbol{z}$	Fabric dilatancy vector
$z_{\max}$	Dilatancy model constant
$\boldsymbol{\alpha}$	Back-stress ratio vector
α	Exponential model constant controlling the bounding surface size
α_{b}	Size of the bounding surface
α_{d}	Size of the dilatancy surface
$\boldsymbol{\alpha}_{\mathrm{hmax}}$	Historic maximum back-stress ratio (i.e. memory) surface
$\boldsymbol{\alpha}_{\mathrm{in}}$	Back-stress ratio vector at initiation of new loading
β	Exponential model constant controlling the dilatancy surface size
$\boldsymbol{\epsilon}_n^{\mathrm{p}}$	Local plastic normal strain vector
$\boldsymbol{\epsilon}_{\mathrm{dev}}^{\mathrm{p}}$	Local plastic deviatoric strain vector
λ	Plastic multiplier
$\boldsymbol{\sigma}^*$	Deviatoric stress tensor
$\boldsymbol{\sigma}_i$	Traction stress vector at the ith sampling plane
σ_n	Magnitude of normal component of $\boldsymbol{\sigma}_i$
$\sigma_{n,\mathrm{dev}}$	Deviatoric part of σ_n
$\sigma_{n,\mathrm{vol}}$	Volumetric part of σ_n
σ_{th}	Threshold normal stress with a default value of 10 kPa
ζ	Dilatancy state parameter

CRediT authorship contribution statement

Hilmi Bayraktaroglu: Writing – original draft, Visualization, Validation, Software, Methodology, Conceptualization. **Mandy Korff:** Writing – review & editing, Supervision, Funding acquisition. **Michael A. Hicks:** Writing – review & editing, Supervision, Project administration, Funding acquisition.

Declaration of competing interest

The authors declare that they have no known competing financial interests or personal relationships that could have appeared to influence the work reported in this paper.

Acknowledgements

This work is part of the research programme DeepNL/SOFTTOP with project number DEEP.NL.2018.006, financed by the Netherlands Organisation for Scientific Research (NWO).

Data availability

Data will be made available on request.

References

Barrero, A.R., Taiebat, M., Dafalias, Y.F., 2020. Modeling cyclic shearing of sands in the semifluidized state. Int. J. Numer. Anal. Methods Geomech. 44 (3), 371–388, URL: https://doi.org/10.1002/nag.3007.

Bayraktaroglu, H., Hicks, M.A., Korff, M., Galavi, V., 2023. A state-dependent multilaminate constitutive model for anisotropic sands. Géotechnique URL: https://doi.org/10.1680/jgeot.22.00165.

Bažant, P., Oh, B.H., 1986. Efficient numerical integration on the surface of a sphere. ZAMM - J. Appl. Math. Mech. / Z. Für Angew. Math. Und Mech. URL: https://doi.org/10.1002/zamm.19860660108.

Boulanger, R.W., Ziotopoulou, K., 2013. Formulation of a sand plasticity plane-strain model for earthquake engineering applications. Soil Dyn. Earthq. Eng. 53, 254–267, URL: https://doi.org/10.1016/j.soildyn.2013.07.006.

Chaudhary, S.K., Kuwano, J., Hashimoto, S., Hayano, Y., Nakamura, Y., 2002. Effects of initial fabric and shearing direction on cyclic deformation characteristics of sand. Soils Found. 42 (1), 147–157, URL: https://doi.org/10.3208/sandf.42.1147.

Cheng, Z., Detournay, C., 2021. Formulation, validation and application of a practice-oriented two-surface plasticity sand model. Comput. Geotech. 132, 103984, URL: https://doi.org/10.1016/j.compgeo.2020.103984.

Cundall, P.A., Strack, O.D.L., 1979. A discrete numerical model for granular assemblies. Géotechnique 29 (1), 47–65, URL: https://doi.org/10.1680/geot.1979.29.1.47.

Dafalias, Y.F., 1986. Bounding surface plasticity. I: mathematical foundation and hypoplasticity. J. Eng. Mech. 112 (9), 966–987, URL: https://doi.org/10.1061/(ASCE)0733-9399(1986)112:9(966).

Dafalias, Y.F., 2016. Must critical state theory be revisited to include fabric effects? Acta Geotech. 11 (3), 479–491, URL: https://doi.org/10.1007/s11440-016-0441-0.

Dafalias, Y., Manzari, M., 2004. Simple plasticity sand model accounting for fabric change effects. J. Eng. Mech. 130 (6), 622–634, URL: https://doi.org/10.1061/(ASCE)0733-9399(2004)130:6(622).

Dafalias, Y.F., Taiebat, M., 2016. SANISAND-z: zero elastic range sand plasticity model. Géotechnique 66 (12), 999–1013, URL: https://doi.org/10.1680/jgeot.15.P.271.

Elgamal, A., Yang, Z., Parra, E., Ragheb, A., 2003. Modeling of cyclic mobility in saturated cohesionless soils. Int. J. Plast. 19 (6), 883–905, URL: https://doi.org/10.1016/S0749-6419(02)00010-4.

Galavi, V., 2007. A Multilaminate Model for Structured Clay Incorporating Inherent Anisotropy and Strain Softening (Ph.D. thesis). Graz, Austria.

Gao, Z., Lu, D., Hou, Y., Li, X., 2023. Constitutive modelling of fabric effect on sand liquefaction. J. Rock Mech. Geotech. Eng. 15 (4), 926–936, URL: https://doi.org/10.1016/j.jrmge.2022.06.002.

Gao, Z., Zhao, J., 2015. Constitutive modeling of anisotropic sand behavior in monotonic and cyclic loading. J. Eng. Mech. 141 (8), 04015017, URL: https://doi.org/10.1061/(ASCE)EM.1943-7889.0000907.

Hasegawa, T., Bažant, Z.P., 1993. Nonlocal microplane concrete model with rate effect and load cycles. I: general formulation. J. Mater. Civ. Eng. 5 (3), 372–393, URL: https://doi.org/10.1061/(ASCE)0899-1561(1993)5:3(372).

Koseki, J., Hoshino, R., Miyashita, Y., Sato, T., 2016. Direct and indirect observations of local deformation properties of saturated sand specimens in undrained cyclic triaxial tests. Jpn. Geotech. Soc. Spec. Publ. URL:.

Lebedev, V., 1976. Quadratures on a sphere. USSR Comput. Math. Math. Phys. URL: https://doi.org/10.1016/0041-5553(76)90100-2.

Li, X.S., Dafalias, Y.F., 2002. Constitutive modeling of inherently anisotropic sand behavior. J. Geotech. Geoenvironmental Eng. 128 (10), 868–880, URL: https://doi.org/10.1061/(ASCE)1090-0241(2002)128:10(868).

Li, X.S., Dafalias, Y.F., 2012. Anisotropic critical state theory: role of fabric. J. Eng. Mech. 138 (3), 263–275, URL: https://doi.org/10.1061/(ASCE)EM.1943-7889.0000324.

Liao, D., Yang, Z.X., 2021. Hypoplastic modeling of anisotropic sand behavior accounting for fabric evolution under monotonic and cyclic loading. Acta Geotech. 16 (7), 2003–2029, URL: https://doi.org/10.1007/s11440-020-01127-z.

Liao, D., Yang, Z., Wang, S., Wu, W., 2022. Hypoplastic model with fabric change effect and semifluidized state for post-liquefaction cyclic behavior of sand. Int. J. Numer. Anal. Methods Geomech. 46 (17), 3154–3177, URL: https://doi.org/10.1002/nag.3444.

Liu, H., Diambra, A., Abell, J.A., Pisanò, F., 2020. Memory-enhanced plasticity modeling of sand behavior under undrained cyclic loading. J. Geotech. Geoenvironmental Eng. 146 (11), 04020122, URL: https://doi.org/10.1061/(ASCE)GT.1943-5606.0002362.

Mitchell, J.K., Soga, K., 2005. Fundamentals of Soil Behavior, third ed. John Wiley & Sons, New York.

Miura, S., Toki, S., 1984. Anisotropy in mechanical properties and its simulation of sands sampled from natural deposits. Soils Found. 24 (3), 69–84, URL: https://doi.org/10.3208/sandf1972.24.3_69.

Nakata, Y., Hyodo, M., Murata, H., Yasufuku, N., 1998. Flow deformation of sands subjected to principal stress rotation. Soils Found. 38 (2), 115–128, URL: https://doi.org/10.3208/sandf.38.2_115.

Nemat, S., Tobita, Y., 1982. Influence of fabric on liquefaction and densification potential of cohesionless sand. Mech. Mater. 1 (1), 43–62, URL: https://doi.org/10.1016/0167-6636(82)90023-0.

Oda, M., Kawamoto, K., Suzuki, K., Fujimori, H., Sato, M., 2001. Microstructural interpretation on reliquefaction of saturated granular soils under cyclic loading. J. Geotech. Geoenvironmental Eng. 127 (5), 416–423, URL: https://doi.org/10.1061/(ASCE)1090-0241(2001)127:5(416).

Pan, K., Xu, T.T., Liao, D., Yang, Z.X., 2022. Failure mechanisms of sand under asymmetrical cyclic loading conditions: experimental observation and constitutive modelling. Géotechnique 72 (2), 162–175, URL: https://doi.org/10.1680/jgeot.20.P.004.

Petalas, A.L., Dafalias, Y.F., Papadimitriou, A.G., 2020. SANISAND-F: sand constitutive model with evolving fabric anisotropy. Int. J. Solids Struct. 188–189, 12–31, URL: https://doi.org/10.1016/j.ijsolstr.2019.09.005.

Pietruszczak, S., Mroz, Z., 2000. Formulation of anisotropic failure criteria incorporating a microstructure tensor. Comput. Geotech. 26 (2), 105–112, URL: https://doi.org/10.1016/S0266-352X(99)00034-8.

Pradhan, T.B., Tatsuoka, F., Sato, Y., 1989. Experimental stress-dilatancy relations of sand subjected to cyclic loading. Soils Found. URL: https://doi.org/10.3208/sandf1972.29.45.

Richart, F.E., Hall, J.R., Woods, R.D., 1970. Vibrations of Soils and Foundations. Prentice Hall, Englewood Cliffs, NJ, USA.

Satake, M., 1978. Constitution of mechanics of granular materials through the graph theory. In: Continuum Mechanical and Statistical Approaches in the Mechanics of Granular Materials. pp. 47–62.

Sivathayalan, S., Logeswaran, P., Manmatharajan, V., 2015. Cyclic resistance of a loose sand subjected to rotation of principal stresses. J. Geotech. Geoenvironmental Eng. 141 (3), 04014113, URL: https://doi.org/10.1061/(ASCE)GT.1943-5606.0001250.

Sivathayalan, S., Vaid, Y.P., 2002. Influence of generalized initial state and principal stress rotation on the undrained response of sands. Can. Geotech. J. 39 (1), 63–76, URL: https://doi.org/10.1139/t01-078.

Taiebat, M., Dafalias, Y.F., 2008. SANISAND: Simple anisotropic sand plasticity model. Int. J. Numer. Anal. Methods Geomech. 32 (8), 915–948, URL: https://doi.org/10.1002/nag.651.

Verdugo, R., Ishihara, K., 1996. The steady state of sandy soils. Soils Found. URL: https://doi.org/10.3208/sandf.36.2_81.

Wan, R.G., Guo, P.J., 1998. A simple constitutive model for granular soils: Modified stress-dilatancy approach. Comput. Geotech. 22 (2), 109–133, URL: https://doi.org/10.1016/S0266-352X(98)00004-4.

Wan, R.G., Guo, P.J., 1999. A pressure and density dependent dilatancy model for granular materials. Soils Found. 39 (6), 1–11, URL: https://doi.org/10.3208/sandf.39.6_1.

Wan, R.G., Guo, P.J., 2001. Effect of microstructure on undrained behaviour of sands. Can. Geotech. J. 38 (1), 16–28, URL: https://doi.org/10.1139/t00-088.

Wan, R.G., Guo, P.J., 2004. Stress dilatancy and fabric dependencies on sand behavior. J. Eng. Mech. 130 (6), 635–645, URL: https://doi.org/10.1061/(ASCE)0733-9399(2004)130:6(635).

Wang, R., Cao, W., Xue, L., Zhang, J.-M., 2020a. An anisotropic plasticity model incorporating fabric evolution for monotonic and cyclic behavior of sand. Acta Geotech. 16, 43–65, URL: https://doi.org/10.1007/s11440-020-00984-y.

Wang, R., Dafalias, Y.F., Fu, P., Zhang, J.-M., 2020b. Fabric evolution and dilatancy within anisotropic critical state theory guided and validated by DEM. Int. J. Solids Struct. 188–189, 210–222, URL: https://doi.org/10.1016/j.ijsolstr.2019.10.013.

Wang, R., Fu, P., Zhang, J.-M., Dafalias, Y.F., 2016. DEM study of fabric features governing undrained post-liquefaction shear deformation of sand. Acta Geotech. 11 (6), 1321–1337, URL: https://doi.org/10.1007/s11440-016-0499-8.

Wang, R., Fu, P., Zhang, J.-M., Dafalias, Y.F., 2019. Fabric characteristics and processes influencing the liquefaction and re-liquefaction of sand. Soil Dyn. Earthq. Eng. 125, 105720, URL: https://doi.org/10.1016/j.soildyn.2019.105720.

Wang, G., Wei, J., 2016. Microstructure evolution of granular soils in cyclic mobility and post-liquefaction process. Granul. Matter 18 (3), 51, URL: https://doi.org/10.1007/s10035-016-0621-5.

Wang, R., Zhang, J.-M., Wang, G., 2014. A unified plasticity model for large post-liquefaction shear deformation of sand. Comput. Geotech. 59, 54–66, URL: https://doi.org/10.1016/j.compgeo.2014.02.008.

Wei, J., Huang, D., Wang, G., 2020. Fabric evolution of granular soils under multidirectional cyclic loading. Acta Geotech. 15 (9), 2529–2543, URL: https://doi.org/10.1007/s11440-020-00942-8.

Wei, J., Wang, G., 2016. Evolution of fabric anisotropy in cyclic liquefaction of sands. J. Micromechanics Mol. Phys. 1 (03n04), 1640005, URL: https://doi.org/10.1142/S2424913016400051.

Wei, J., Wang, G., 2017. Discrete-element method analysis of initial fabric effects on pre- and post-liquefaction behavior of sands. Géotechnique Lett. 7 (2), 161–166, URL: https://doi.org/10.1680/jgele.16.00147.

Yamada, S., Takamori, T., Sato, K., 2010. Effects on reliquefaction resistance produced by changes in anisotropy during liquefaction. Soils Found. 50 (1), 9–25, URL: https://doi.org/10.3208/sandf.50.9.

Yang, S., Huang, D., 2022. Fabric evolution and liquefaction resistance in multiple-liquefaction process: a micromechanical study using DEM-clump. Acta Geotech. 17 (12), 5655–5674, URL: https://doi.org/10.1007/s11440-022-01645-y.

Yang, S., Huang, D., Wang, G., Jin, F., 2022c. Probing fabric evolution and reliquefaction resistance of sands using discrete-element modeling. J. Eng. Mech. 148 (6), 04022023, URL: https://doi.org/10.1061/(ASCE)EM.1943-7889.0002104.

Yang, M., Taiebat, M., Dafalias, Y.F., 2022a. SANISAND-MSf: a sand plasticity model with memory surface and semifluidised state. Géotechnique 72 (3), 227–246, URL: https://doi.org/10.1680/jgeot.19.P.363.

Yang, M., Taiebat, M., Radjai, F., 2022b. Liquefaction of granular materials in constant-volume cyclic shearing: transition between solid-like and fluid-like states. Comput. Geotech. 148, 104800, URL: https://doi.org/10.1016/j.compgeo.2022.104800.

Yang, Z.X., Xu, T.T., Chen, Y.N., 2018. Unified modeling of the influence of consolidation conditions on monotonic soil response considering fabric evolution. J. Eng. Mech. 144 (8), 04018073, URL: https://doi.org/10.1061/(ASCE)EM.1943-7889.0001499.

Yoshimine, M., Ishihara, K., Vargas, W., 1998. Effects of principal stress direction and intermediate principal stress on undrained shear behavior of sand. Soils Found. 38 (3), 179–188, URL: https://doi.org/10.3208/sandf.38.3_179.

Zhang, J.-M., 1997. Cyclic Critical Stress State Theory of Sand with Its Application to Geotechnical Problems (Ph.D. thesis). Tokyo Institute of Technology, URL: https://ci.nii.ac.jp/naid/500000165212.

Zhang, J.-M., Wang, G., 2012. Large post-liquefaction deformation of sand, part I: physical mechanism, constitutive description and numerical algorithm. Acta Geotech. 7 (2), 69–113, URL: https://doi.org/10.1007/s11440-011-0150-7.

Zou, Y., Liu, H., 2021. Modeling liquefaction-induced large deformation of sand incorporating the effects of fabric anisotropy evolution. J. Eng. Mech. 147 (10), 04021072, URL: https://doi.org/10.1061/(ASCE)EM.1943-7889.0001946.